Instant fabrication and selection of folded structures using drop impact

Arnaud Antkowiak [*], Basile Audoly [*], Christophe Josserand [*], Sébastien Neukirch [*]   and Marco Rivetti [*]

[*]CNRS & UPMC Univ Paris 06, UMR 7190: Institut Jean Le Rond d'Alembert, 4 place Jussieu, F-75005 Paris, France

A drop impacting a target cut out in a thin polymer film is wrapped by the film in a dynamic sequence involving both capillary forces and inertia. Different 3D structures can be produced from a given target by slightly varying the impact parameters. A simplified model for a nonlinear dynamic Elastica coupled with a drop successfully explains this shape selection, and yields detailed quantitative agreement with experiments. This first venture into the largely unexplored dynamics of elasto-capillary assemblies opens up the perspective of mass production of 3D packages with individual shape selection.

Capillary forces exerted by a water drop are sufficient to strongly deform thin elastic objects such as carbon nanotubes or biological filaments [1, 2] or even to wrinkle thin polymer sheets [3]. Elasto-capillary interactions are abundant in Nature and are responsible for phenomena such as lung airway collapse [4] and the clustering of insect bristles [5, 6]. They are relevant to a number of applications at the micrometer or nanometer scale, such as MEMS [7, 8, 9], mass production of non-spherical lenses [10], or drug delivery [11]. On the other hand, drop impact is one of the most common illustration of fluid mechanics in everyday life, having practical applications as diverse as pesticide delivery [12] or polymer inkjet printing for flexible electronics [13]. Impact and splash of droplets have been studied for more than a century but only a few studies have addressed the case of a compliant substrate, and those are limited to small deformations [14]. Here, the impact of a drop on a very flexible target is used to produce millimeter-size three-dimensional structures instantly. We show that impact allows a gain of five orders of magnitude in the fabrication time as compared to a previous method based on evaporation [15]; in addition, we unveil the possibility to select the shape of the structure, by tuning the impact parameters. When scaled down and combined with inkjet technology that operates at similar dimensionless numbers, this set-up opens up the possibility of mass production of individualized 3D packings at the submillimetric scale.

In our experiments, the flexible targets are cut out from thin PDMS sheets. Such polymer films, naturally exhibiting a non-wetting behavior with a water contact angle close to $110°$, are treated to enhance contact line pinning (see Methods for fabrication details). The target is laid down on a super-hydrophobic surface, which by repelling water confines the drop onto the target. A water drop of controlled volume is released from a given height, thereby allowing control of the impact velocity. For well-chosen impact parameters, we observe the formation of an instant capillary origami. This is demonstrated in the experiment of figure 1,
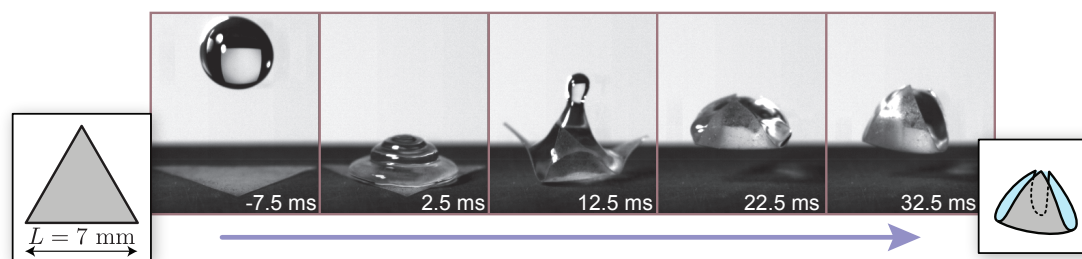
Figure 1. Instant capillary origami, obtained with a water droplet of radius $R = 1.55$ mm impacting a thin triangular polymer sheet with thickness $h = 55$ μm at velocity $U = 0.53$ m$\cdot$s^{-1}. This time sequence reveals that encapsulation results from the interplay between the motion of fluid interface by capillary forces, and the large, dynamic deformations of the film.

where a drop impacts at its center a triangular target of width 7 mm with velocity $U = 0.53$ m$\cdot$s^{-1}. Just after impact, the drop spreads out over the target up to a maximal extent where inertia is balanced by the restoring action of capillarity. Next, surface tension drives a flow towards the center of the drop. This causes the rebound of the drop [16], and of the elastic film that sticks to it. While in free fall above the ground, the elastic sheet quickly wraps the drop. An elasto-capillary bundle with a tetrahedral shape is formed, and falls down to the ground. The whole sequence takes place in 40 ms, which is the typical duration of an hydrophobic rebound [16].

When mediated by drop impact, encapsulation is thus considerably faster than when driven by evaporation [15] which typically requires half an hour.

Formation of the instant origami is governed by several lengthscales. Let $B = E h^3/(12(1-\nu^2))$ be the bending modulus of the film, E its Young's modulus, ν its Poisson's ratio, $h = 55 \ \mu$m its thickness, L its length, $\mu = 51.8 \, 10^{-3} \ \mathrm{kg \, m^{-2}}$ its mass per unit area, g the acceleration of gravity, and $\gamma = 72$ mN.m^{-1} and $\rho = 1000$ kg.m^{-3} the fluid's surface tension and density. In all our experiments, the initial drop radius is $R = 1.55$ mm. Wrapping into a tightly packed structure is made possible by the fact that this radius R is both smaller than the gravito-capillary length $\ell_{\mathrm{gc}} = (\gamma/\rho g)^{1/2} \simeq 2.7$ mm

for the drop to remain spherical, and larger than the elasto-capillary length $\ell_{\mathrm{ec}} = (B/\gamma)^{1/2} \simeq 0.55$ mm above which capillary forces can make slender objects buckle [1, 6, 15]. In addition, gravity is important as the size L of the target is millimetric, and comparable to the elasto-gravitational length $\ell_{\mathrm{eg}} = (B/(\mu \, g))^{1/3} \simeq 3.5$ mm above which gravity bends a cantilever beam. These lengthscales are all relevant, and comparable: encapsulation results from the mixed effects of gravity, elasticity and capillarity.

Drop impact, more than just speeding up elasto-capillary wrapping, also allows for final shape control. A typical illustration of this shape selection mechanism is presented in figure 2, and in Supplemental movies S2 and S3.
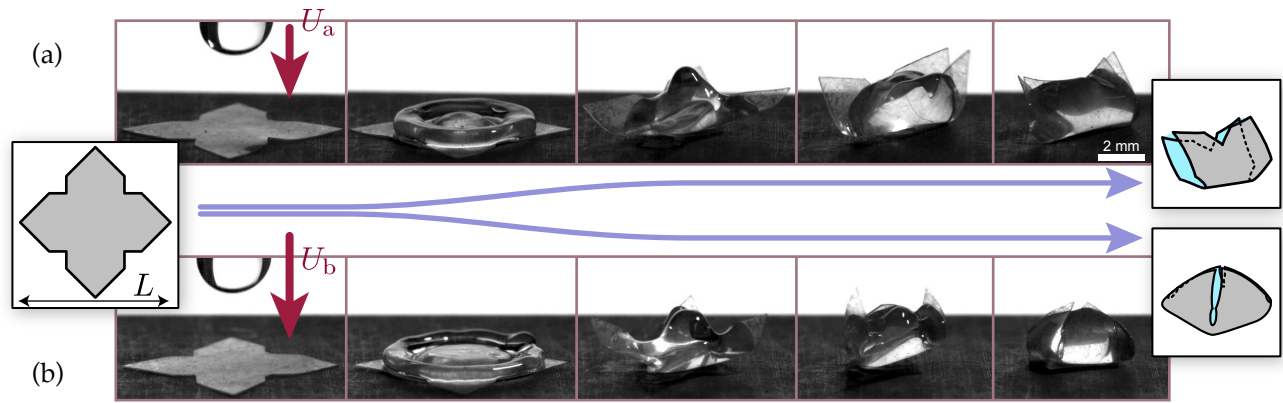

Figure 2. A flower-shaped target reveals the possibility of pattern selection based on impact velocity U. Radius of the drop is $R = 1.55$ mm in both experiments, target width is $L = 10$ mm and $U_{\mathrm{b}} > U_{\mathrm{a}}$. *(a)* For low impact velocity, $U_{\mathrm{a}} = 0.68 \ \mathrm{m \cdot s^{-1}}$, a cylindrical bundle is formed, having two-fold symmetry. *(b)* At higher velocity, $U_{\mathrm{b}} = 0.92 \ \mathrm{m \cdot s^{-1}}$, the drop spreads more widely and almost wets the entire surface of the film; a pyramidal wrap is formed, having four-fold symmetry.

In this experiment, a drop impacts a small flower-shaped film at its center. For a fixed drop radius, different folding scenarios can be observed depending on the impact velocity. At low impact speed, spreading of the drop is limited, and the final pattern is the cylindrical folding of figure 2a. At higher speeds, the drop quickly embraces the entire surface of the sheet, and upon retraction a pyramidal wrap is obtained, see figure 2b. Different instant origamis can thus be obtained by simply tuning the velocity of impact. A similar selection can be observed with other target shapes. In the case of rectangular films, we observed a competition between two folding modes, one along the length of the rectangle and another one

along its width. The pattern can be selected by varying not only the velocity but also the position of impact. The role of these two parameters is investigated in detail next.

The phenomenon of dynamic elasto-capillary encapsulation can be carried over to a 2D geometry where it is considerably simpler to analyze. We carried out a series of systematic experiments using as a target a long and narrow rectangular strip of width $w = 2$ mm, length $L = 5$ cm, such that $h \ll w \ll L$. For this narrow strip, $L/\ell_{\mathrm{eg}} = 14.3$. This 2D setting is sketched in figure 3a. First it simplifies the geometry by suppressing the 3D aspects of folding such as the formation of singular cones and ridges visible in the final frame in figure 2b. Secondly it separates the fluid and solid time scales, as we show next.
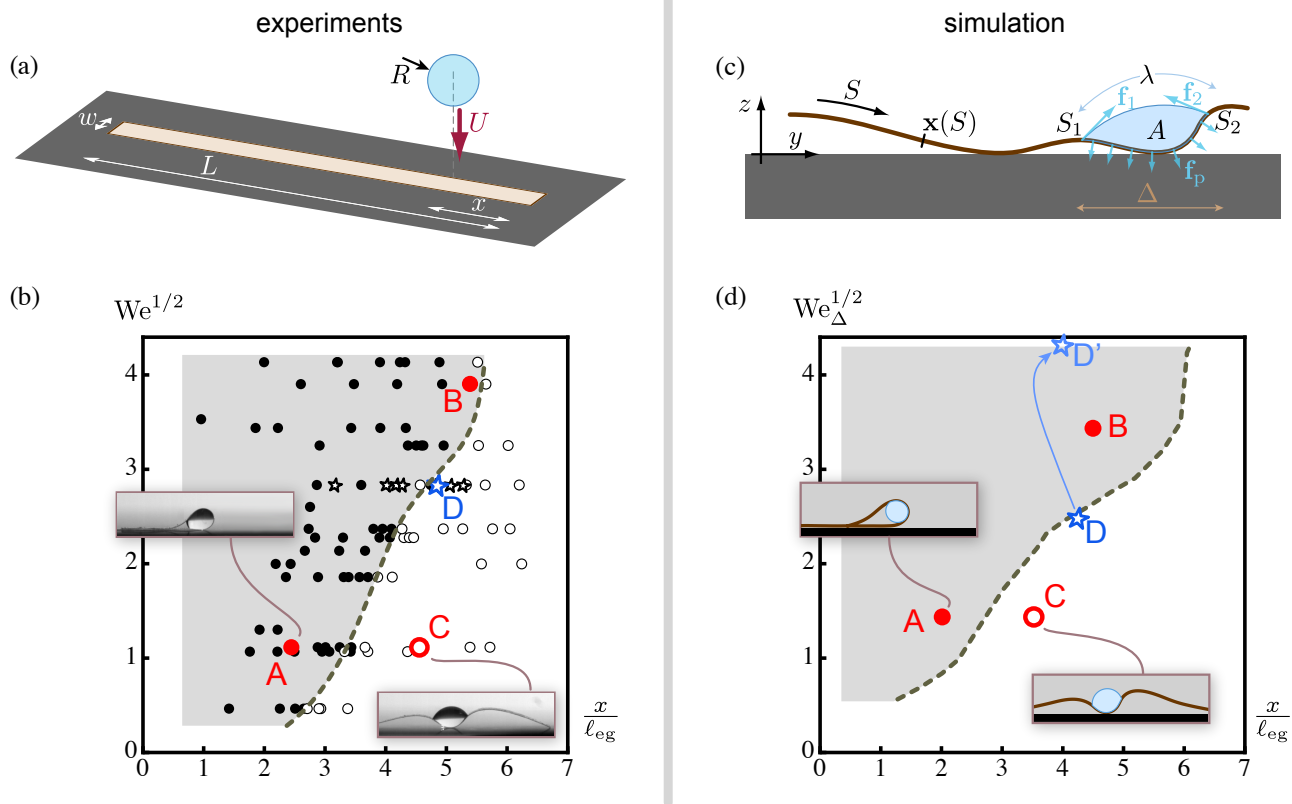
Figure 3. Comparison of experiments (a,b) and simulations (c,d) in a 2D geometry. (a) In these experiments, a drop impacts a long, thin polymer strip laying down on a substrate, at a variable distance x from its end, and with variable impact velocity U. Strip dimensions are $L = 5$ cm and $w = 2$ mm, and drop radius is $R = 1.55$ mm. (b) Phase diagram showing the outcome of the experiment: non-encapsulated drop (open circles), encapsulated drop (filled dots), or encapsulated drop with the help of a secondary drop obtained by pinch-off (stars). (c) Numerical model of a 2D dynamic Elastica coupled with a quasi-static, incompressible fluid with surface tension. (d) Phase diagram for the Elastica model. In (b,d), typical final shapes are shown in inset. The time sequences of a few selected experiments, labelled A, B, C and D here, are compared in figures 4 and 5. During the simulation run labelled D in (d), the impact parameters are changed to account for the capture of a secondary drop, as shown by the light blue arrow.

Remarkably, shape selection can still be observed in 2D: the phase diagram in figure 3b reveals a competition between wrapped and non-wrapped final configurations. This diagram was obtained by systematically varying the distance x from the point of impact to the end of the strip, and the impact velocity U. For the purpose of plotting, the position of impact x was measured in units of $\ell_{\rm eg}$, and U in units of the capillary velocity $(\gamma/\rho R)^{1/2}$: the resulting dimensionless velocity is the square root of the Weber number $\mathrm{We} = \rho\, U^2\, R/\gamma$. In our experiments, the Weber number varies [1] from 0.21 to 15, which is the typical value at which the inkjet technology operates.

Qualitatively, the process of encapsulation requires passing a gravitational energy barrier with the aid of the initial kinetic energy. The outcome of a particular experiment reflects the efficiency of this energy transfer. Indeed, since both L and R are larger than $\ell_{\rm ec}$, the strip is flexible enough to bend around the drop and the energy is always minimum in the encapsulated state. However, for drops that are too slow, or

impact too far from the edge, the barrier associated with lifting up the strip prevents the system from reaching this global minimum. When the drop is deposited near the end (small x), encapsulation involves lifting a short segment of the strip, making the barrier lower. For small enough values of x, encapsulation can even be observed after nearly quasi-static deposition of the drop. For larger values of x, however, the barrier is higher and some amount of kinetic energy is required. This explains the existence of a threshold for the velocity U allowing encapsulation, and the increase of this threshold with x. This qualitative reasoning is consistent with the orientation of the boundary obtained in the experimental diagram, see figure 3b. It is now turned into a fully quantitative model. This requires to first analyze the timescales.

---

[1] For the volume of the drop to be well controlled, the drop should not touch the target before it detaches from the syringe. This sets a minimal release height, corresponding to a lower bound $\mathrm{We} = 0.21$ in the experiments.

During the fast initial spreading of the drop, part of the incident kinetic energy is quickly and irreversibly transferred into surface energy. Irreversibility is here a consequence of contact line pinning: due to the roughness of the substrate, the contact line never recedes. It remains anchored to its maximal extent in all our experiments. This maximal extent, denoted Δ, is directly set by the impact parameters. It is a key mechanical quantity that determines how the capillary forces are distributed, and how efficiently they bend the film during the subsequent folding. Δ was measured in a separate series of experiments using the same film (See Supplementary material S1). We found that, in our range of parameters, spreading is well described by the empirical law $\frac{\Delta(U)-\Delta_0}{2\,R} = 0.32\,\mathrm{We}^{1/2}$. The parameter $\Delta_0 = \Delta(U=0)$ represents the amount of spreading for quasi-static deposition, as we are in partial wetting conditions. Note that the exponent $1/2$ is consistent with a conversion of kinetic energy $\sim \rho\,U^2\,R^3$ into surface energy $\sim \gamma\,\Delta^2$. A simple scaling analysis explains why the spreading takes place on a much faster time scale, denoted τ_c, than the time scale τ_e for the subsequent elastic deformation. The capillary timescale $\tau_\mathrm{c} = \sqrt{\rho R^3/\gamma}$ is independent of the impact velocity [16]. By contrast, the elastic time scale is given by the natural period of vibration of the free end of the strip, $\tau_\mathrm{e} \sim x^2 \left(\frac{\mu}{B}\right)^{1/2}$. The ratio $\frac{\tau_\mathrm{c}}{\tau_\mathrm{e}} \sim \left(\frac{R^3}{\ell_\mathrm{gc}{}^2\,\ell_\mathrm{eg}}\right)^{1/2} \Big/ (x/\ell_\mathrm{eg})^2 \sim 0.02$ is small, when evaluated with the typical value $x = 4\,\ell_\mathrm{eg}$ of the 2D experiments.

With the aim to predict encapsulation, we consider a mechanical model for the slow folding dynamics of the strip following the initial drop spreading. In this model, the two contact lines are anchored and separated by a prescribed curvilinear distance Δ. The value of Δ captures the initial transfer of kinetic into surface energy, and the rest of the motion is driven solely by capillary forces. The dynamics of the strip is governed by the following potential energy:

$$\mathcal{U} = \int_0^L \left[\frac{\hat{B}}{2}\,|\mathbf{x}''(S,t)|^2 + \hat{\mu}\,g\,\mathbf{x}(S,t)\cdot\mathbf{e}_z \right] \mathrm{d}S + \hat{\gamma}\,\lambda(\mathbf{x}(\cdot,t),A,x,\Delta)$$

$$[\mathbf{1}]$$

and kinetic energy:

$$\mathcal{T} = \frac{1}{2} \int_0^L \hat{\mu}\,|\dot{\mathbf{x}}(S,t)|^2\,\mathrm{d}S.$$

$$[\mathbf{2}]$$

Here, S is the arc-length along the strip ($0 \leq S \leq L$), and $\mathbf{x}(S,t)$ is the position of the centerline. Deformations take place in the (x,z) plane, and $\mathbf{e}_z$ is the unit vector pointing upwards. Dots denote derivation with respect to time, and primes with respect to arc-length S. The integrals in the potential and kinetic energies $\mathcal{U}$ and $\mathcal{T}$ are the classical ones for an elastic curve of bending modulus $\hat{B} = (Bw)$ and mass per unit length $\hat{\mu} = (\mu\,w)$, subjected to gravity g: the two first terms in $\mathcal{U}$ are the elastic energy of bending, proportional to curvature squared, and the potential energy due to gravity. Coupling with the fluid is achieved by the capillary energy $(\hat{\gamma}\,\lambda)$, where $\hat{\gamma} = (\gamma\,w)$ is the line tension of the fluid-air interface and λ its perimeter, see figure 3c. This interface contacts the strip at points whose arclength coordinates S_1 and S_2 are prescribed in terms of two impact parameters, x and Δ:

$S_1 = L - x - \Delta/2$ and $S_2 = L - x + \Delta/2$. Owing to the separation of time scales $\tau_\mathrm{c} \ll \tau_\mathrm{e}$, the drop is treated quasi-statically. For any configuration of the strip $\mathbf{x}(S,t)$, the shape of the drop is found by minimizing the interfacial length λ under the constraint of a prescribed area A. The result is a circular cap attached to the fixed endpoints S_1 and S_2, whose radius and perimeter λ can be computed geometrically in terms of the current configuration of the strip: $\lambda = \lambda(\mathbf{x}(\cdot,t),A,x,\Delta)$ (see Supplementary material S1).

Our numerical code integrates in time the equations of motion obtained by applying Lagrangian mechanics to our Lagrangian $\mathcal{L} = \mathcal{T} - \mathcal{U}$. In deriving these equations, we consider the inextensibility constraint $|\mathbf{x}'| = 1$ and the presence of an impenetrable ground $\mathbf{x}\cdot\mathbf{e}_z \geq 0$. Fluid incompressibility is used during the reconstruction of $\lambda(\mathbf{x}(\cdot,t),A,x,\Delta)$. The resulting equations of motion are the classical equations for the dynamics of a 2D Elastica subjected to gravity forces, to frictionless reaction from the ground in the event of contact, and to capillary forces (See Supplementary material S1 for details). The capillary forces tend to make the potential energy $\mathcal{U}$ lower. They do so by bending the strip around the drop, thereby reducing the interfacial length λ while preserving the imposed area A.

The numerical phase diagram in figure 3d has been obtained by varying the impact parameters systematically in a series of simulation runs. The positions of the endpoints S_1 and S_2 of the wet region were sampled, restricted to $0 < S_1 < S_2 < L$. In each simulation run, the values of S_1 and S_2 are recorded, as well as the outcome of the numerical experiment, encapsulated or non-encapsulated (the exact criterion for encapsulation is described in the Methods section). Each pair of values S_1 and S_2 is translated into impact parameters $\Delta = |S_2 - S_1|$ and $x = L - \frac{S_1+S_2}{2}$. For the purpose of comparison with the experiments, the impact parameter Δ is then converted into an equivalent Weber number using our empirical law $\mathrm{We}_\Delta^{1/2} := (\Delta(U) - \Delta_0)/(0.64R)$ capturing the fast initial spreading of the drop. As revealed by the phase diagram in figure 3d, the model successfully explains the selection of the final shape by the impact parameters. The essential features of the experimental diagram are reproduced. Any value of the position of the center of impact x is associated with a critical value of the Weber number. This corresponds to a minimal value of the velocity U (or the spreading Δ) for encapsulation to occur. In addition, this critical value of the Weber number is an increasing function of x. The numerical model is based on simplifying approximations such as neglecting the weight and inertia of the drop, as well as three dimensional effects, capillary waves and depinning of the contact line. Such a depinning occurs on rare occasions, as in the final frames of figure 4A and 4B. We obtain nevertheless a close agreement on the boundaries between the encapsulated and non-encapsulated regions. The simulation parameters are set directly from their experimental values and there is no adjustable parameter.

The model not only predicts the final shape of the strip but also its detailed time evolution. Comparison of typical experimental and numerical time sequences is shown in figure 4 for selected values of the impact parameters. An excellent, frame by frame agreement is obtained.
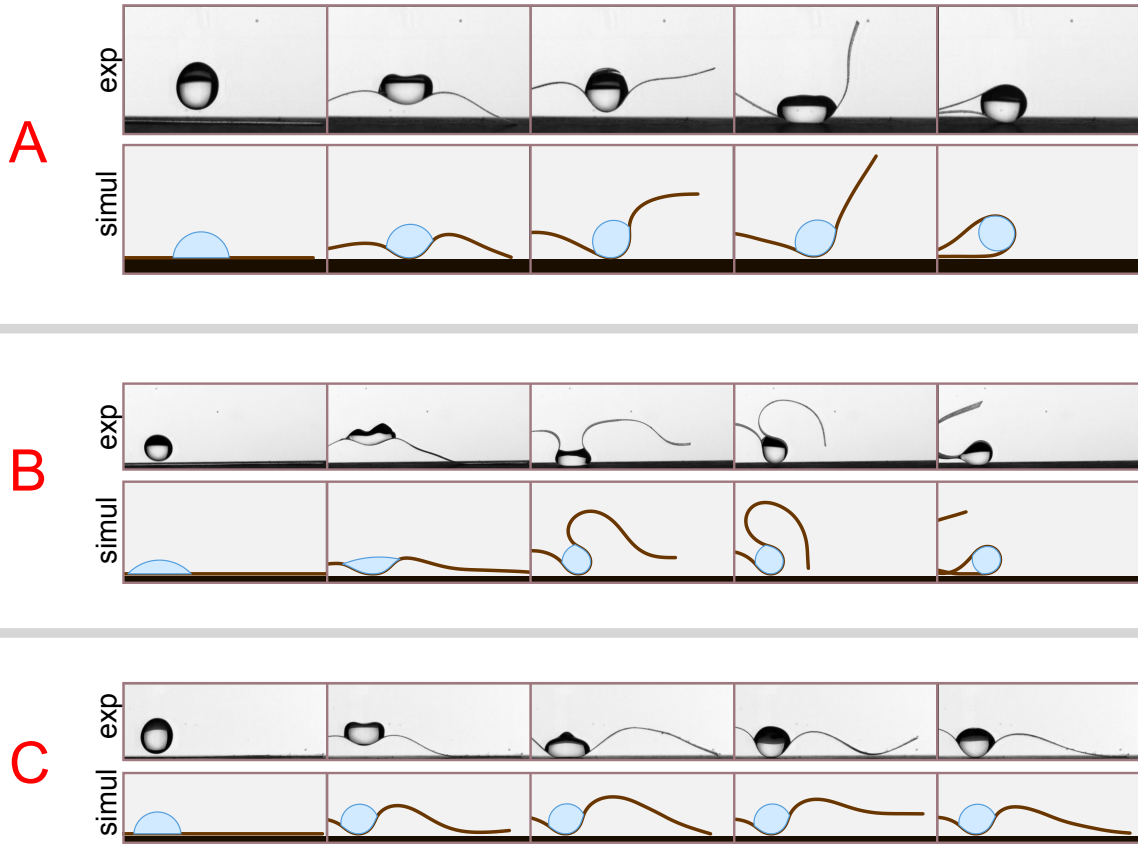
Figure 4. Comparison of experimental and simulated time sequences for selected impact parameters shown in figure 3. Only a fraction of the strip is shown here. (A) 'Rigid' encapsulation observed when $x/\ell_{\mathrm{eg}} \lesssim 1$. (B) 'Floppy' encapsulation: for larger values of x/ℓ_{eg}, the free end of the film folds so as to mitigate the penalization due to gravity. (C) When the drop is deposited too far from the end of the strip, capillary forces cannot overcome the weight of the strip and the drop remains unencapsulated. See also supplementary movie S3.

The sets of impact parameters values were chosen so as to illustrate the main regimes of encapsulation. The model perfectly reproduces both the 'rigid' mode of encapsulation in sequence A, where the free end of the strip folds about the drop with little deformation, the 'floppy' mode in sequence B reminiscent of the Fosbury-flop, where bending of the strip helps reducing the height of the gravitational energy barrier, and the absence of encapsulation in sequence C, when impact occurs further from the endpoint of the strip than in A and with a lower velocity U (and spreading length Δ) than in B. To compensate for the slightly different shape of the boundary in the experimental and numerical phase diagrams, the points A, B and C have been moved by a small amount in the numerical diagram, *i. e.* we have assigned them the same position relative to the boundary as in the experimental diagram, rather than the same absolute position. Overall, all the details of the dynamic sequence leading to encapsulation are captured with remarkable accuracy.

For a small subset of the experiments, confined to a limited region of the experimental phase diagram and labelled by stars in figure 3b, encapsulation takes a special route. In this region, the final state is not always reproducible even for fixed impact parameters. In addition, encapsulation can be observed for anomalously large values of x: the two stars to the right of the point D in figure 3b clearly stand out to the right of the boundary. This surprising behaviour can be explained by looking at the time sequence in figure 5a.
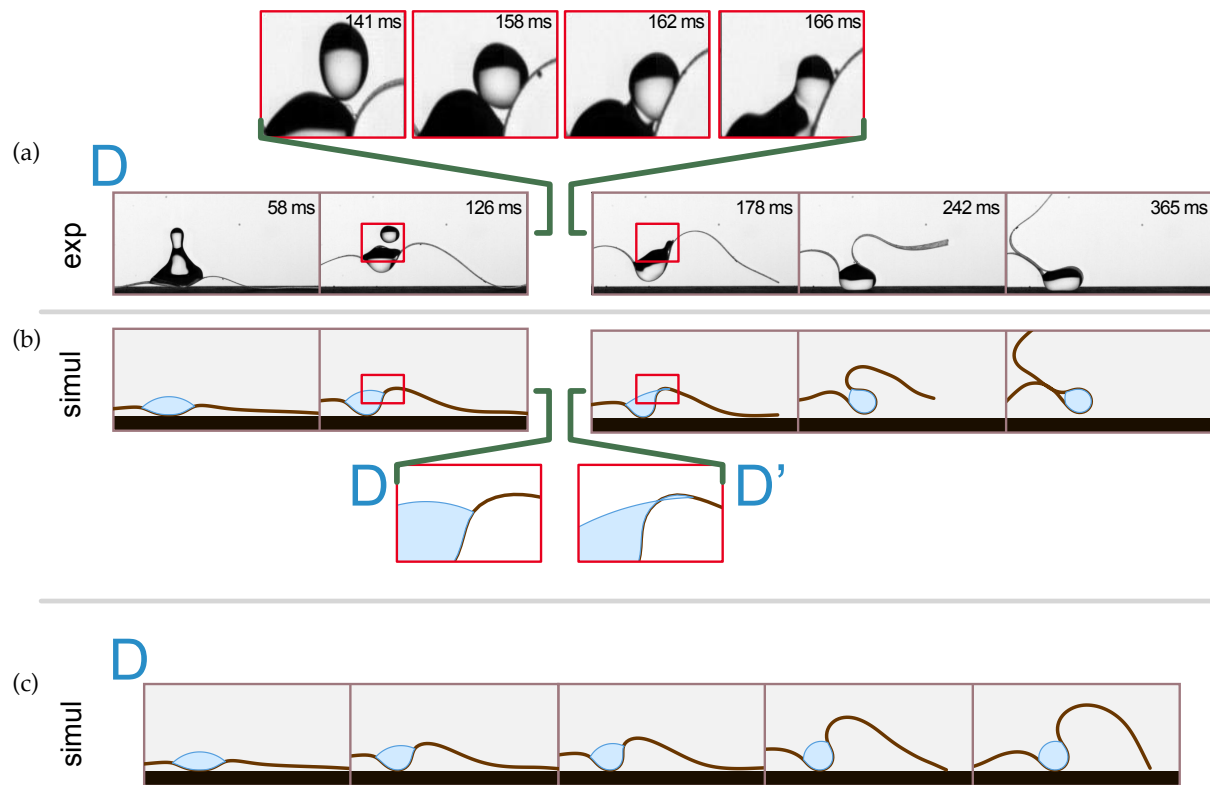
Figure 5. Encapsulation aided by a topology change of the drop. (a) In the experiments a secondary drop appears transiently by pinch-off and coalescence when $\mathrm{We}^{\frac{1}{2}} \approx 2.8$. This detachment leads to encapsulation in a region where it would otherwise not be possible: the impact parameters for this experiment are denoted by the star labelled D, located to the right of the boundary in the phase diagram of figure 3b. (b) This transient topology change is accounted for by extending the footprint Δ of the drop in the middle of the simulation (inset D'), by an amount measured from the experimental frames. As a result, simulation correctly predicts encapsulation, and matches the experimental movie frame by frame. (c) When this footprint Δ is left unchanged, simulation fails to predict encapsulation.

Shortly after the initial spreading, a vertical jet is formed and a secondary drop detaches. Under the action of gravity, it accelerates downwards, catches up with the falling capillary bundle, and coalesces. In some experiments, such as that labelled D in the figure, the bouncing drop lands on the edge of the main drop and coalesces, thereby increasing the wet length Δ. This induces a redistribution of the capillary forces that substantially modifies the subsequent folding dynamics. Since the ejection of a secondary drop is ruled by the Weber number, this view is consistent with the observation that anomalous encapsulation events are all observed when the Weber number is close to a particular value, $\mathrm{We}^{1/2} \approx 2.8$. When the simulation is run as earlier, ignoring the secondary drop, encapsulation is not correctly predicted, as shown in figure 5c. The role of the secondary drop is captured by a simple extension of the model. From the experimental movies, we measure the time of ejection of the secondary drop and the position S_2' of the contact line after coalescence. This yields virtual impact parameters, labelled D' in figure 3d, which are indeed well inside the region of encapsulation. We run again the simulation, now updating the position S_2 of the contact line to

S_2' at the time of coalescence. As shown in figure 5b, the key role of the secondary drop on the final pattern is accurately captured. Encapsulation is correctly predicted and comparison with the experiments reveals an excellent, frame by frame agreement.

Our system demonstrates one of the interesting and largely unexplored phenomena arising out of the combination of capillarity with large, dynamic deformations of fluid interfaces and flexible bodies. At small scales, viscosity and capillarity are often considered as dominant, and inertia negligible. The impact of a drop is an interesting exception to this rule: kinetic energy, when initially stored in the form of a rigid-body mode of translation, cannot be dissipated by viscosity. This energy ends up in selecting the final shape among competing equilibria. We studied in detail a 2D setting, where well-controlled experiments were found in quantitative agreement with a tractable model. In this 2D setting, multistability arises from gravity. The dynamical shape selection uncovered here works also at smaller scales, where gravity becomes unimportant. Indeed, there are other sources of multistability, such as nonlinear elasticity of thin films or the follower character of capillary forces. As a matter of fact, numerical experiments

confirmed the persistence of shape selection in the absence of gravity (see Supplementary Material S1 and supplementary video S4). Robustness of the selection mechanism opens up the perspective of scaling down the experiment to the size of an inkjet drop.

Materials and Methods

The thin elastic sheets were made of polydimethylsyloxane (PDMS - RTV) that was spin coated on a glass microscope slide at 1500 RPM, and cured at 70° C for one hour. The resulting thickness was 55 μm. The thin polymer films were peeled off from the glass using a surgical blade, and further cut out to the desired shape. The pattern was then deposited onto a rigid copper substrate warranting a high restitution coefficient upon impact. To make the copper super-hydrophobic we used electroless galvanization [17]: it was first coated with a textured metallic layer ($AgNO_3$) and then covered with a low surface energy self-assembled monolayer (1H,1H,2H,2H-perfluorodecanethiol - HDFT). The polymer patterns were powdered with talc to prevent self-adhesion; talc was found to enhance contact line pinning. All sequences were recorded using a high-speed camera Photron SA-5 at 5000 fps.

The numerical simulations are based on the 'Discrete Elastic Rods' model of Bergou *et al.* [18], which has been validated against analytical reference solutions in the original paper. Here, we used it in a 2D geometry where twist is absent. We used the codebase developed by M. Bergou and E. Grinspun at Columbia University,

which has kindly been made available to us. Its robust and efficient treatment of the inextensibility constraint allows for fast simulations, taking typically less than 30 s even at the highest resolution. Details on the implementation of our model are provided in Supplementary material S1. In the simulations, we used the experimental values of $\hat{\mu} = \mu\, w$, $\hat{B} = B\, w$ and $\hat{\gamma} = \gamma\, w$ for the meniscus force, and we set $A = V/\ell_{\text{eg}}$. This choice of A reflects the observation that the rounded shape of the drop makes it wider than w; as a result, its width is clearly closer to ℓ_{eg} than to w. These experimental values were made dimensionless, as we used units such that gravity g, lineic mass $\hat{\mu}$ and bending modulus $\hat{B}$ all have the value 1. In such units, the line tension $\hat{\gamma}^* = 40$. and the area of the 2D drop is $A^* = 0.36$.

The criterion for encapsulation used both in experiments and numerical simulations was to test whether the endpoint of the free edge $S = L$ had been moved to the left of the point at the center of impact $S = L - x$: encapsulation corresponds to $y(L, t = \infty) < y(L - x, t = \infty)$.

1. Cohen A. E., Mahadevan L. (2003) Kinks, rings, and rackets in filamentous structures. Proc Natl Acad Sci USA 100:12141–12146

2. Chakrapani N., Wei B., Carrillo A., Ajayan P. M., Kane R. S. (2004) Capillarity-driven assembly of two-dimensional cellular carbon nanotube foams. Proc Natl Acad Sci USA 101:4009–4012

3. Huang J. et al. (2007) Capillary Wrinkling of Floating Thin Polymer Films. Science 317:650–653

4. Heil M. (1999) Minimal liquid bridges in non-axisymmetrically buckled elastic tubes. J Fluid Mech 380:309–337

5. Eisner T., Aneshansley D. J. (2000) Defense by foot adhesion in a beetle (Hemisphaerota cyanea). Proc Natl Acad Sci USA 97:6568–6573

6. Bico J., Roman B., Moulin L., Boudaoud A. (2004) Adhesion: Elastocapillary coalescence in wet hair. Nature 432:690

7. Syms, R.R.A., Yeatman, E.M., Bright, V.M., Whitesides, G.M. (2003) Surface tension-powered self-assembly of microstructures – the state-of-the-art. Journal of Microelectromechanical Systems 12:387–417

8. Leong, Timothy G., Lester, Paul A., Koh, Travis L., Call, Emma K., Gracias, David H. (2007) Surface Tension-Driven Self-Folding Polyhedra. Langmuir 23:8747–8751

9. Raccurt O., Tardif F., d'Avitaya F. A., Vareine T. (2004) Influence of liquid surface tension on stiction of SOI MEMS. Journal of Micromechanics and Microengineering 14:1083

10. O'Neill F. T., Sheridan J. T. (2002) Photoresist reflow method of microlens production Part I: Background and experiments. Optik - International Journal for Light and Electron Optics 113:391–404

11. Soppimath K. S., Aminabhavi T. M., Kulkarni A. R., Rudzinski W. E. (2001) Biodegradable polymeric nanoparticles as drug delivery devices. Journal of Controlled Release 70:1–20

12. Rein M. (1993) Phenomena of liquid drop impact on solid and liquid surfaces. Fluid Dynamics Research 12:61–93

13. de Gans B. J., Duineveld P., Schubert U. (2004) Inkjet Printing of Polymers: State of the Art and Future Developments. Advanced Materials 16, 203–213

14. Pepper R. E., Courbin L., Stone H. A. (2008) Splashing on elastic membranes: The importance of early-time dynamics. Physics of Fluids 20:082103–8

15. Py C., Reverdy P., Doppler L., Bico J., Roman B., Baroud C. N. (2007) Capillary Origami: Spontaneous Wrapping of a Droplet with an Elastic Sheet. Phys. Rev. Lett. 98:156103

16. Richard D., Clanet C., Quere D. (2002) Surface phenomena: Contact time of a bouncing drop. Nature 417:811

17. Larmour I. A., Bell S. E. J., Saunders G. C. (2007) Remarkably Simple Fabrication of Superhydrophobic Surfaces Using Electroless Galvanic Deposition. Angewandte Chemie 119:1740–1742

18. Bergou M., Wardetzky M., Robinson S., Audoly B., Grinspun E. (2008) Discrete Elastic Rods. ACM Transactions on Graphics 27:63

Instant fabrication and selection of folded structures using drop impact
Supplementary material

Arnaud Antkowiak [*] , **Basile Audoly** [*] , **Christophe Josserand** [*] , **Sébastien Neukirch** [*]   and **Marco Rivetti** [*]

[*]CNRS & UPMC Univ Paris 06, UMR 7190: Institut Jean Le Rond d'Alembert, 4 place Jussieu, F-75005 Paris, France

Experimental law for the fast initial spreading

We conducted a series of experiments with the aim to characterize the spreading Δ of an impacting drop on the same thin and narrow polymer strip as used in our '2D' experiments. Here, both the drop radius R and the impacting velocity U are varied. The results are reported in figure 1. The relative spreading $(\Delta - \Delta_0)/2R$ is plotted as a function of the Weber number $\mathrm{We} = \rho U^2 R/\gamma$. Here, Δ_0 represents the spreading in a quasi-static setting, when the drop is gently deposited on the flexible strip. The value of Δ_0 is extrapolated from the dataset and not measured directly; we find $\Delta_0 = 2.04$, 2.20, 1.96, 3.68 mm for $R = 1.2$, 1.5, 1.6, 1.85 mm respectively. The data for the different radii R all collapse on a single curve, indicating that the Weber number We is the relevant parameter for the spreading. A simple power law fits the data:

$$\frac{\Delta - \Delta_0}{2\,R} = 0.32\,\mathrm{We}^{1/2}, \qquad [\mathbf{1}]$$

as shown in the figure.
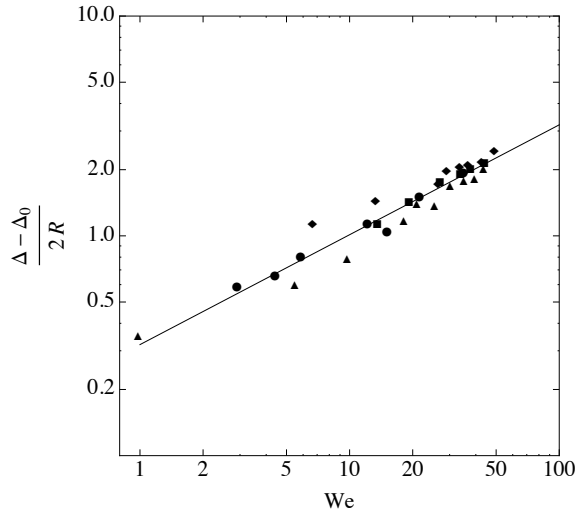
Figure 1. Spreading of a drop on a polymer strip. Different drop radii were used : $R = 1.2$ mm (▲), 1.5 mm (●), 1.6 mm (■) and 1.85 mm (♦). The dimensionless spreading length $(\Delta - \Delta_0)/2R$ is plotted as a function of the Weber number $\mathrm{We} = \rho U^2 R/\gamma$. The solid line is given by equation (1).

This experimental law is valid in our particular range of parameters. Its practical use is to allow confrontation of the experiments, where the velocity U is available, with the simulations, where the spreading length Δ is prescribed.

Calculation of fluid forces in the numerical code

Equations for dynamic, 2D Elastica. Let S be the arclength, t the time, and $\mathbf{x}(S,t)$ be the unknown position of centerline, see figure 2. The inextensibility condition writes $|\mathbf{x}'(S,t)| = 1$. Let then $\mathbf{t}(S,t)$ and $\mathbf{q}(S,t)$ be the unit tangent and normal to the centerline, respectively:

$$\mathbf{t}(S,t) = \mathbf{x}'(S,t), \qquad \mathbf{q}(S,t) = (-\mathbf{e}_y) \times \mathbf{t}(S,t). \qquad [\mathbf{2a}]$$

Note that with these sign conventions, the local basis $(\mathbf{t}, \mathbf{q})$ is orthonormal and direct in the plane (x, z).

Figure 2. Geometry of a 2D Elastica

The signed curvature is defined by

$$\kappa(S,t) = \mathbf{x}''(S,t) \cdot \mathbf{q}(S,t). \qquad [\mathbf{2b}]$$

We consider a linearly elastic, naturally straight strip with bending modulus $\hat{B}$. Its constitutive relation expresses proportionality between the curvature strain κ and the bending moment: $\mathbf{m}(S,t) = \hat{B}\,\kappa(S,t)\,(-\mathbf{e}_y)$. By the Kirchhoff equation for the balance of moment, $\mathbf{m}' + \mathbf{t} \times \mathbf{n} = 0$, the internal moment $\mathbf{m}$ has to be balanced by an internal force $\mathbf{n}$ of the form:

$$\mathbf{n}(S,t) = T(S,t)\,\mathbf{t}(S,t) - \hat{B}\,\kappa'(S,t)\,\mathbf{q}(S,t), \qquad [\mathbf{2c}]$$

where the tension T is an unknown Lagrange multiplier associated with the inextensibility condition. The second Kirchhoff equation expresses the fundamental law of dynamics:

$$\hat{\mu}\,\ddot{\mathbf{x}}(S,t) = \mathbf{n}'(S,t) + \mathbf{p}(S,t). \qquad [\mathbf{2d}]$$

Here, $\mathbf{p}(S,t)$ is the density of applied force, per unit length of the rod. Inserting equations (2a–2c) into equation (2d), we

---

Reserved for Publication Footnotes

obtain a nonlinear partial differential equation for the main unknown $\mathbf{x}(S,t)$ which is fourth order in space and second order in time. This is the classical equation for a dynamic Elastica in 2D. This equation of motion can be obtained by variational principles from the Lagrangian $\mathcal{L} = \mathcal{T} - \mathcal{U}$ given in main text, see for instance Ref. [1].

Quasi-static reconstruction of the drop. At every time, we determine the shape of the drop given the profile $\mathbf{x}(S)$ of the centerline — the time variable is omitted in the present Section. The shape of the drop is determined by the following requirements, see figure 3:
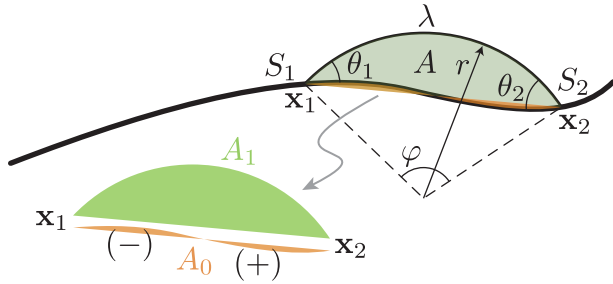
Figure 3. Quasi-static reconstruction of the fluid domain.

(i) the fluid-air interface is anchored to two points in space $\mathbf{x}_1 = \mathbf{x}(S_1)$ and $\mathbf{x}_2 = \mathbf{x}(S_2)$ that are prescribed, (ii) the length λ of this interface has to be minimal to make the capillary energy $(\hat{\gamma}\,\lambda)$ minimum, (iii) the area of the fluid, $i.\,e.$ of the region enclosed by the fluid-air interface and by the wet part of the rod $\mathbf{x}(S)$ for $S_1 \leq S \leq S_2$, is constrained to a prescribed value A. The mass of fluid is neglected. This approximation suppresses capillary waves, and is consistent with the fact that the simulation resolves the elastic timescale τ_{e}, which is much larger than the capillary one, τ_{c}, see main text.

This constrained variational problem characterizes the equilibrium shape of a wetting fluid without gravity. Its solution is classical: the fluid-air interface is an arc of circle at equilibrium. The properties of this arc are determined as follows. First, we compute the signed area A_0 of the region enclosed between between the wet part of the rod, traced out by $\mathbf{x}(S)$ for $S_1 \leq S \leq S_2$, and the segment joining $\mathbf{x}_1$ and $\mathbf{x}_2$, with the sign conventions shown in figure 3. The area A_1 of the circular cap shown in green in the figure, enclosed between the fluid-air interface and the segment $[\mathbf{x}_1, \mathbf{x}_2]$, is $A_1 = A - A_0$. The angle φ of the circular cap is then calculated by solving the following geometric relation:

$$\frac{A_1}{|\mathbf{x}_1\mathbf{x}_2|^2} = \frac{\varphi - \sin\varphi}{8\,\sin^2\frac{\varphi}{2}}.$$

The radius r and the perimeter λ of the circular cap are then found by

$$r = \frac{|\mathbf{x}_1\mathbf{x}_2|}{2\,\sin\frac{\varphi}{2}}, \qquad \lambda = \varphi\,r.$$

Finally, the angles θ_1 and θ_2 of the fluid-air interface with respect to the local frame $(\mathbf{t}, \mathbf{q})$ are given by

$$\theta_1 = \frac{\varphi}{2} + \angle(\mathbf{t}_1, \mathbf{x}_2 - \mathbf{x}_1), \qquad \theta_2 = \frac{\varphi}{2} + \angle(\mathbf{x}_1 - \mathbf{x}_2, -\mathbf{t}_2),$$

where $\angle(\mathbf{a}, \mathbf{b})$ denotes the signed measure of the angle made by the vectors $\mathbf{a}$ and $\mathbf{b}$, and $\mathbf{t}_1 = \mathbf{x}'(S_1) = \mathbf{t}(S_1)$ and $\mathbf{t}_2 = \mathbf{x}'(S_2) = \mathbf{t}(S_2)$ denote the unit tangents at the two

points of contact of the interface with the rod. Note that the angles θ_1 and θ_2 are different from the equilibrium value set by the Young-Dupré relation since the contact line is pinned.

In the simulation we do not implement any mechanism preventing the fluid-air interface from crossing the rod. A spurious crossing is visible in the inset labelled D$'$ in fig. 5b of main text. Overlooking the collisions of the fluid-air interface with the rod is justified *a posteriori* by the fact that we observed such collisions in only one instance, which is precisely the simulation labelled D $-$ D$'$. Even then the crossing took place during a short time interval, just after the anchor point S_2 was moved to the right. In addition this crossing takes place over a region much smaller than the size of the drop. As a result, its impact on the simulation is very limited.

Expression of forces. We consider three types of forces, with total lineic density $\mathbf{p}(S,t)$:

$$\mathbf{p}(S,t) = \mathbf{p}_{\mathrm{g}}(S,t) + \mathbf{p}_{\mathrm{c}}(S,t) + \mathbf{p}_\gamma(S,t), \qquad \textbf{[3]}$$

where $\mathbf{p}_{\mathrm{g}}$ denotes the weight of the Elastica, $\mathbf{p}_{\mathrm{c}}$ the reaction of the support, and $\mathbf{p}_\gamma$ the capillary forces.

The weight is given in terms of the mass per unit length $\hat{\mu}$:

$$\mathbf{p}_{\mathrm{g}}(S,t) = -\hat{\mu}\,\mathbf{e}_z. \qquad \textbf{[4]}$$

In the absence of friction on the ground, the contact force reads:

$$\mathbf{p}_{\mathrm{c}}(S,t) = p_{\mathrm{c}}(S,t)\,\mathbf{e}_z \qquad \textbf{[5]}$$

where $p_{\mathrm{c}} \geq 0$ is the unknown contact pressure with the ground. This force is associated with the unilateral constraint $\mathbf{x}(S)\cdot\mathbf{e}_z \geq 0$. Note that $p_{\mathrm{c}} = 0$ when there is no contact, $i.\,e.$ $\mathbf{x}(S)\cdot\mathbf{e}_z > 0$. In the implementation, we avoid calculating the contact pressure p_{c} as collision response is treated using an impulse-based model.

The capillary force is made up of two point-like forces, acting at the points of contact S_1 and S_2 and represented by Dirac distributions, and a distributed force arising from the capillary pressure inside the drop:

$$\mathbf{p}_\gamma(S,t) = \mathbf{f}_1\,\delta(S - S_1) + \mathbf{f}_2\,\delta(S - S_2)$$
$$+ \mathbf{f}_{\mathrm{p}}(S)\,H(S - S_1)\,H(S_2 - S), \quad \textbf{[6]}$$

where the Heaviside function H is used here to restrict the support of the last term to the wet region, $S_1 < S < S_2$. The point-like forces $\mathbf{f}_1$ and $\mathbf{f}_2$ are directed along the fluid-air interface, and represent line tension:

$$\mathbf{f}_1 = \hat{\gamma}\,(\mathbf{t}(S_1)\,\cos\theta_1 + \mathbf{q}(S_1)\,\sin\theta_1), \qquad \textbf{[7a]}$$
$$\mathbf{f}_2 = \hat{\gamma}\,(-\mathbf{t}(S_2)\,\cos\theta_2 + \mathbf{q}(S_2)\,\sin\theta_2). \qquad \textbf{[7b]}$$

The distributed force $\mathbf{f}_p$ is the pressure force arising from capillary pressure

$$\mathbf{f}_p(S) = -\frac{\hat{\gamma}}{r}\,\mathbf{q}(S). \qquad \textbf{[8]}$$

These capillary forces can be derived from the capillary energy $(\hat{\gamma}\,\lambda)$ by variational principles.

Selection of final shape in the absence of gravity

Here we show that the final pattern can be selected by the impact velocity even in the absence of gravity. Gravity was considered in the main text as it allows to set up well-controlled experiments showing quantitative agreement with the numerics.

Figure 5 shows time sequences for two numerical experiments with the same parameters, except for the spreading Δ. Figure (5a) makes use of a smaller spreading length
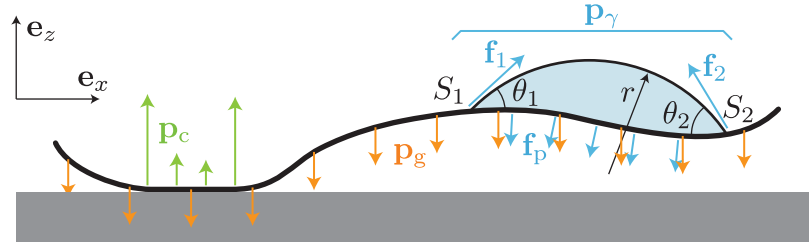
Figure 4. Forces applied on the elastic filament: capillary forces $\mathbf{p}_\gamma$, weight $\mathbf{p}_g$, and contact forces from the support $\mathbf{p}_c$.
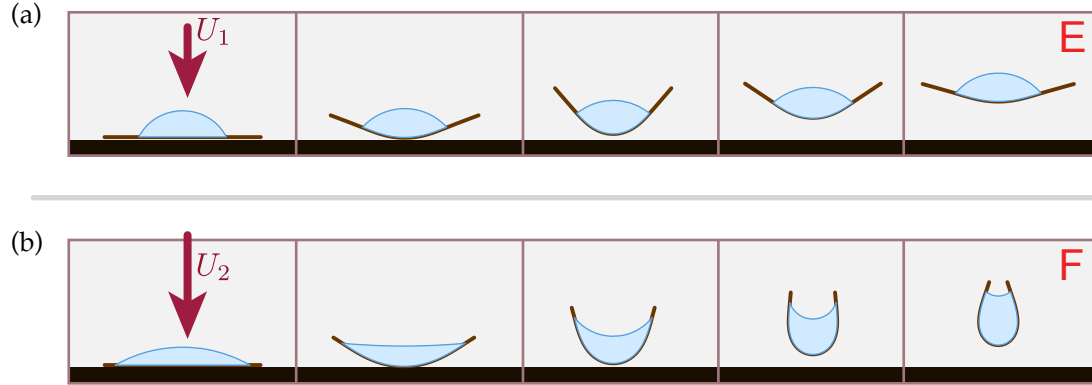

Figure 5. Time sequences illustrating selection in the absence of gravity: by increasing the spreading length without modifying the other parameters, the final state goes from (a) unencapsulated to (b) encapsulated. Parameters common to both simulations are rescaled drop area $A/\ell_{ec}^2 = 1.5$ and rod length $L/\ell_{ec} = 4.6$. A small damping is enforced using a viscous drag coefficient per unit length $\mathrm{d}b/\mathrm{d}s = 1.04\,(\hat{\mu}\,\hat{B})/\ell_{ec}^2$. Different drop impacts are simulated using (a) $\Delta/\ell_{ec} = 2.5$ for a slower impact and (b) $\Delta/\ell_{ec} = 4$ for a slower impact. Overall duration of the time sequences is $t = 8.4\,(\hat{\mu}/\hat{B})^{1/2}$. See also supplementary movie S4.

$\Delta = 2.5\,\ell_{ec}$, corresponding to a slower impact velocity, than in figure (5b), for which $\Delta = 4\,\ell_{ec}$. Encapsulation is observed with the larger spreading length only, leading to the same findings as in the experiments of Figure 2 in main text (dynamic impact on a flower-shaped target without long arms).

The possibility of a transition from unencapsulated to encapsulated final states can be understood by looking at the branches of equilibria for fixed rod length L, drop area A and elasto-capillary length ℓ_{ec}. These branches are plotted in figure 6 for the same parameters as used in the time sequences of figure 5. A bistability is observed for some values of spreading length Δ, as in reference [2]. For sufficiently large spreading width Δ, the kinetic energy of the impacting drop is converted into capillary energy (captured by the numerical parameter Δ) and back into kinetic energy, allowing the bun-

dle to jump onto the encapsulated branch from an initially flat configuration.
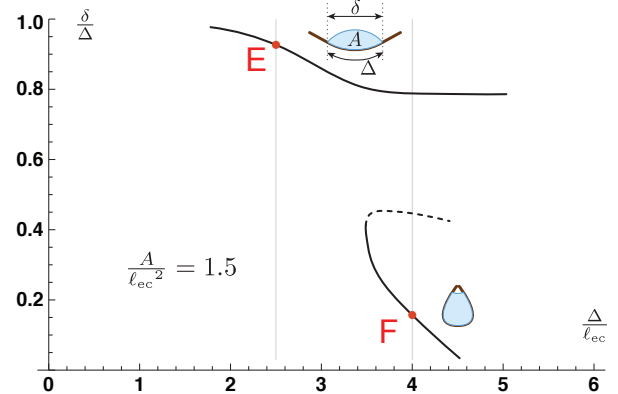
Figure 6. Equilibrium configurations in the absence of gravity, for $A/\ell_{ec}^2 = 1.5$ and $L/\ell_{ec} = 4.6$ (same parameters as in figure 5). The x axis is the rescaled length Δ of the fluid-solid interface, and the y axis measures encapsulation. For some values of the parameters, multiple equilibrium configurations are in competition.

1. B. Audoly and Y. Pomeau, Elasticity and geometry: from hair curls to the nonlinear response of shells (Oxford University Press, 2010).

2. Py C., Reverdy P., Doppler L., Bico J., Roman B., Baroud C. N. (2007) Capillary Origami: Spontaneous Wrapping of a Droplet with an Elastic Sheet. Phys. Rev. Lett. 98:156103